A Scalable optical meta-surface glazing design for agricultural greenhouses

Physica Scripta

PAPER

A Scalable optical meta-surface glazing design for agricultural greenhouses

Venkatasubramanian Lakshminarayanan, Mostafa Ranjbar, Khalifa Aliyu Ibrahim and Zhenhua Luo

School of Water, Energy, and Environment, Cranfield University, Cranfield, United Kingdom

E-mail: z.luo@cranfield.ac.uk

OPEN ACCESS

RECEIVED
15 November 2023

REVISED
10 January 2024

ACCEPTED FOR PUBLICATION
31 January 2024

PUBLISHED
16 February 2024

Keywords: FDTD (finite difference time domain), thin films, optical metamaterials, low-emissivity, plasmonic, nanoparticle, glazing

Abstract

Optical meta-surfaces allow controllable reflection and transmission spectra in both optical and infrared regions. In this study, we explore their potential in enhancing the performance of low-emission glazing designed for improved energy efficiency, for agricultural greenhouses in cold climates. The low-emission glazing employs thin film optics to retain heat by allowing solar radiation while reflecting radiation emitted by room-temperature objects. The incorporation of metamaterials that can be scalably manufactured and designed for capturing solar energy in the mid-infrared spectrum, offers an opportunity to further enhance the glazing's energy efficiency. Based on existing literature, the finite difference time domain (FDTD) method and the transfer matrix method are utilised to propose a metamaterial structure, with spherical silver nanoparticles and thin-films. We compare the performance of this proposed design against existing materials. The outcome of this study offers insights into the potential of metamaterials in optimizing the energy efficiency of cold-climate agricultural greenhouses.

1. Introduction

Greenhouse agricultural production takes advantage of a controlled climate inside the greenhouses to improve the production and quality of crops. This also enables throughout the year cultivation of crops which are not otherwise possible [1]. Greenhouses have various energy demands including heating, cooling, humidification, shading and lighting systems to optimise plant growth [2].

In colder climates heating accounts for up to 90% of the operational costs [3]. This energy is supplied by fossil fuel contributing to greenhouse gas emissions. This also impacts the economics of the agricultural business due to the volatile nature of energy costs [4]. Greenhouse glazing is often designed to allow the transmittance of solar radiation for heating and photosynthesis while preventing heat loss by reflecting the far infrared frequencies reducing heat loss [5, 6].

Metamaterials and meta-surfaces have been successfully applied in various industrial application [7–10]. Optical metamaterials have specifically been developed for many glazing purposes [11, 12], The aim is to improve the performance of existing greenhouse glazing designs.

Electromagnetic metamaterials refer to engineered materials with optical characteristics such as negative permittivity and permeability that are not found in natural materials. This is achieved by engineering structures or units smaller or near the working wavelength. These units are often arranged in a periodic or a random structure throughout the material to create homogeneous material and properties. Such materials are useful in many applications such as glazing design for heating as well as cooling, optical sensing of various properties, controlled polarisation, and even stealth applications [7, 8, 11, 13, 14]. The engineered structures allow for tuneable optical properties such as even negative refractive indices.

Metasurfaces are 2D metamaterial structures that can be developed to improve/tune transmittance, reflectance, absorption, and polarisation properties of glazing and other surfaces. Selective polarisation with

gold helix structure, Selective IR reflectance with silver disk shaped nanoparticles, polymer sheets with SiO_2 particles for radiative cooling glazing are some of the examples of metamaterial structures in literature used in glazing application [7, 11, 12].

Producing such structures at optical frequencies presents significant challenges as very precise methods are required since the structures are in subwavelength sizes [15]. Two distinct approaches to fabricating metamaterials and meta-surfaces are the top-down and bottom-up approaches. In the top-down approach advanced techniques like electron beam lithography, direct laser writing, and interference lithography are often used to produce well defined and complex structures [7, 16]. In the alternative bottom-up approach, the structures are assembled into the required arrangement from units/metaatoms i.e., nanoparticles. This approach provides several advantages such as a better ability to fabricate bulk materials with high scalability and cost effectiveness [17]. Such techniques have been used to produce effective glazing structures to meet various needs [11, 12, 18]. Using such novel designs suited for bottom-up fabrication techniques, it is possible to control the reflectivity and admittance characteristics and to improve the suitability of glazing material for cold environments.

In this article, we present a novel optical meta-surface design that can enhance the performance of the greenhouse glazing applications. It can be produced using bottom-up approach. This design is achievable through a bottom-up approach. Its performance was computationally assessed using finite difference time domain (FDTD) and transfer matrix methods (TMM), with a comparative against current glazing structures in cold environments. The advantages and disadvantages of the proposed design was also discussed.

2. Modelling and simulation

The solar irradiance spectrum varies at various locations on earth mainly depending on the latitude and various weather conditions. In this work, the standard ASTM G137 spectrum is used to evaluate solar cells and other meta-surface designs. This is known as the AM1.5 spectrum [19, 20].

Plank's law for black body radiation is shown in equation (1). It describes the emission spectra of a perfectly emissive surface (black body) as a function of temperature. The emissivity of plants can be approximated to a black body. The plant body and leaves can be considered in equilibrium with the surrounding air [21].

$$E(\lambda, T) = \frac{2hc_0}{\lambda^5}\frac{1}{e^{\left(\frac{hc}{\lambda KT}\right)} - 1} \tag{1}$$

$$E - Emissive\ power\left(\frac{W}{m^2.Sr.Hz}\right)$$

$$c_0 - Speed\ of\ light\ in\ vaccum\left(2.9979\frac{m}{s}\right)$$

$$h - Plank's\ constant\,(6.62607015 \times 10^{-34})$$

$$K - Boltzman\ constant\left(1.380649 \times 10^{-23}\,\frac{J}{K}\right)$$

$$\lambda - wavelength\ of\ radiation(m)$$

$$T - Black - body\ Temperture(K)$$

Figure 1 shows the normalized spectral power distributions for black body radiation at 300K along with the solar irradiance spectrum (AM1.5). The photosynthetically active (PAR) region i.e., 400 nm–700 nm is also labelled [22]. Most of the emissive power for blackbody radiation at 25 °C is between 3 to 35 μm.

2.1. Existing glazing systems

Low-e (low emissivity) coatings are designed to have high reflectance in the infrared spectrum, thus preventing radiation heat loss from inside the greenhouse/building through the glazing. Silver thin film manufactured by sputtering is the most popular type of low-e glazing. Silver thin films are based on the Drude model of dielectrics which states that the emissivity of a material correlates strongly with its resistivity.

The thickness, surface finish and the grain structure are the most important factors affecting the performance of thin films. The thickness of the silver layer varies from 5nm to 20 nm [19]. The coated glass is often used in a double-pane design for maximum thermal insulation. Other materials such as gold layers and semiconductors (Indium Titanium Oxide, Flourine-doped tin Oxide) based low-e glass also exist. However, silver exhibits the best performance in terms of low emissivity in the infrared (IR) spectrum and also high visible light transmittance [23].

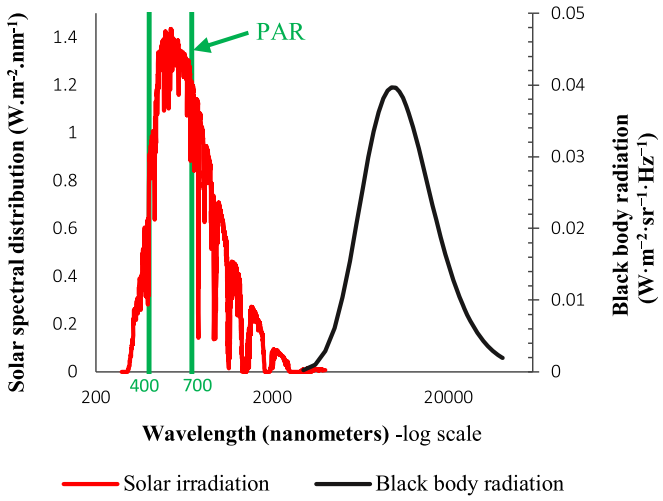

Figure 1. Solar spectrum and black body radiation spectrum (PAR—Photosynthetically active region for plants).

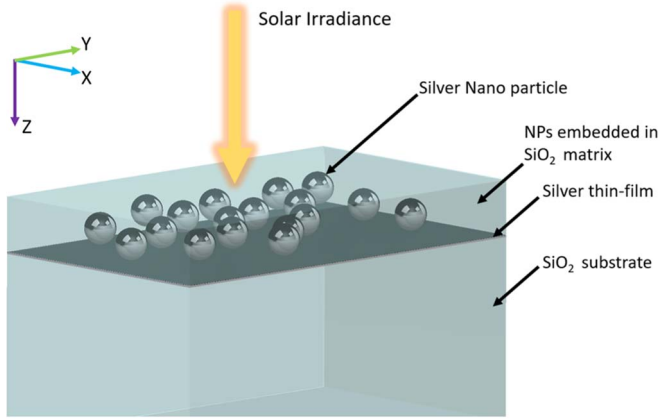

Figure 2. Conceptual rendering of the proposed metamaterial design (not to scale).

2.2. Meta-surface low-e design

The silver thin film design provides good reflection in the IR region. However, about 50% of the solar energy is available in the Near Infrared (NIR) (700 nm to 2800 nm). The silver thin film coating exhibits high reflectance in this spectrum thereby wasting a significant part of the incoming solar irradiation. There is a potential to improve the IR admittance of Ag thin film low-e glazing using metamaterial structures as demonstrated by [19].

In our work, we addated unstructured metamaterials with nano-particles (NPs). It is intented to improve the absorption in the solar frequencies by creating strong resonance and field intensification at the silver metal surface using a silver thin film structure. It is worthy to mention that designs with strong absorption peak at 700nm with the extension into the infrared region has already been produced by the other researchers [19]. This enables greater admittance thereby capturing more of the available incident solar energy.

We target similar performance using spherical silver NPs and strong controllable resonance in the frequencies of interest [24]. This should improve manufacturability enabling its application in glazing as shown by [11, 18]. A layer of spherical silver NPs embedded in a matrix of SiO_2 applied on top of the metal thin-film layer facing outside in double-pane configuration. The proposed novel metamaterial design is shown in figure 3. The size of Ag NPs can be controlled while it is embedded in SiO_2 matrix [25]. Embedding of NPs in a transparent matrix in other polymers has reported in [11, 18]. The conceptual render of the metamaterial is depicted in figure 2.

The proposed design is compared against silver thin-film of thickness 8nm using the same simulation setup. The parameters for evaluation were NP size, NP density, and the distance to the thin film layer. The initial values of the parameters are reported in table 1. The silver NPs of 150 nm diameter is considered for a broad spectral response and activity in the infrared region based on Mie theory [26]. The centre distance to the thin film layer is

Table 1. Initial parameters for analysis.

Parameter	Initial value
NP diameter	150 nm
Distance from thin film i.e., x/r	1.57
Fill factor	25%

selected to match the silver square design by [19]. All the parameters are varied to understand the general trend with respect to the performance of the glazing [19].

2.3. Design formulation

Equations (2) to (5) show the maxwell's equations for the propagation of EM waves in the cartesian coordinates. The constitutive relations for linear isotropic dispersive materials in the time domain is mentioned in equations (6) and (7). Most materials show large variations in permeability for different frequencies of field excitations i.e., electro-magnetic waves.

$$\nabla \times \boldsymbol{H} = \boldsymbol{J} + \frac{\partial \boldsymbol{D}}{\partial t} \tag{2}$$

$$\nabla \times \boldsymbol{E} = -\frac{\partial \boldsymbol{B}}{\partial t} \tag{3}$$

$$\nabla.\boldsymbol{D} = \rho \tag{4}$$

$$\nabla.\boldsymbol{B} = 0 \tag{5}$$

where,

$$\mathbf{D}(\mathrm{t}) = \varepsilon(t) \ * \ \boldsymbol{E}(t) \tag{6}$$

$$\mathbf{B}(\mathrm{t}) = \mu(t) \ * \ \boldsymbol{H}(t) \tag{7}$$

$\boldsymbol{E}$ - Electric field vector
$\boldsymbol{H}$ - Magnetic field intensity vector
$\boldsymbol{B}$-Magnetic flux density
D-electric flux density
ρ-Charge density

By substituting equations (4) and (5) in equations (6) and (7) respectively and changing to the frequency domain using Fourier transform gives equations (8) and (9).

$$\nabla \times \boldsymbol{H} = \varepsilon(\omega) j\omega \boldsymbol{E} \tag{8}$$

$$\nabla \times \boldsymbol{E} = -j\omega\mu(\omega)\boldsymbol{H} \tag{9}$$

For materials with loss (i.e., absorption of energy by attenuation of EM waves) in the frequency domain, the permeability is a complex value, i.e., $\varepsilon = \varepsilon' + j\varepsilon''$. The imaginary component of the permeability models the decay of the electric field amplitude as the wave propagates through the lossy medium. The imaginary part of ε'' is equal to σ/ω. It is the conductivity of the material.

The refractive index is the ratio of wave velocities in the medium versus the speed of light in free space c_0. It is given by relative permeability and relative permittivity ε_r and μ_r and shown in equations (10) to (13). Here μ_r is also known as the extinction coefficient.

$$n' = \sqrt{\varepsilon_r \mu_r} \tag{10}$$

$$\varepsilon = \varepsilon_r \varepsilon_0 \tag{11}$$

$$\mu = \mu_r \mu_0 \tag{12}$$

$$n' = n + jk \tag{13}$$

Material properties databases such as the Refractive index database, compiles the properties of the materials including refractive index and extinction coefficients. This data can used for analysis. All the materials considered, i.e., silver, lime glass and air are non-magnetic i.e., μ_r is equal to one [27].

Many natural and metamaterials often produce different response at different frequencies. The variation is often non-linear. A number of analytical models have been developed to model the refractive indices for natural as well as metamaterials. A few examples of them are discussed below.

Cauchy equation is an empirical model which can model refractive indices of glasses and gasses shown in equation (14). A,B,C , etc are empirical constants [28].

$$n(\lambda) = A + \frac{B}{\lambda^2} + \frac{C}{\lambda^4} + \ldots \tag{14}$$

Sellmeier equation is an improved model over the Cauchy equation capable of modelling more complex dispersion. It shown in equation (15). Here A_i and B_i are material dependant constants [28].

$$n^2(\lambda) = 1 + \sum_i \frac{A_i}{(\lambda^2 - B_i)} \tag{15}$$

The Lorentz model of lossy dielectric oscillators is capable modelling many real-world materials such as metals, transparent materials as well as resonant metamaterials. This is shown in equation (16) [29].

$$n^2(\omega) = 1 + \frac{\omega_p^2}{\omega_0^2 - \omega^2 - i\omega\gamma} \tag{16}$$

ω_p^2—Effective plasma frequency of the material
ω_0— Natural frequency of the oscillators
γ—Damping coefficient (often chosen empirically)
ω—frequency of incident light

Apart from these examples more complex models exist to estimate the refractive index of materials. However, for metamaterials these characteristics are tuned based on structure of the material and often undergo complex resonance effects which cannot be modelled analytically. Simulations and experimentation are used to determine the effective refractive indices in the frequencies of interest.

2.4. Analysis methodology

The maxwells equations are solved at the material interfaces to know the reflection and transmission spectrum of the material. Finite Difference Time Domain simulations and Transfer Matrix Method were used to analyse and validate the proposed design. In general, part of the incident light waves reflect, and the remaining transmit through various absorptive and dielectric media with complex refractive indices. The phase-shifted waves interfere at the optical boundaries. They are leading to spectrally selective reflection and transmittance. They can be controlled by varying the thickness and the material of different layers [30].

The Fresnel coefficients relate the amplitude of the electric fields of the wave travelling into and out of each layer boundary. The relations are written in a matrix form for each layer in equation (17). The general form for m-layers is formulated in equation (18) in which C_1 to C_m are the characteristic transfer matrices for each layer.

$$\begin{bmatrix} E_{m-1}^+ \\ E_{m-1}^- \end{bmatrix} = \frac{1}{t_m} \begin{bmatrix} e^{i\delta_{m-1}} & r_m e^{i\delta_{m-1}} \\ r_m e^{-i\delta_{m-1}} & e^{-i\delta_{m-1}} \end{bmatrix} \begin{bmatrix} E_m^+ \\ E_m^- \end{bmatrix} \tag{17}$$

$$\begin{bmatrix} E_0^+ \\ E_0^- \end{bmatrix} = \frac{C_1 C_2 \ldots . C_m}{t_1 t_1 \ldots t_m} \begin{bmatrix} E_m^+ \\ E_m^- \end{bmatrix} \tag{18}$$

where,

$$\delta_m = \frac{2\pi}{\lambda}(n_m - ik_{m-1})d_{m-1} \tag{19}$$

where d_m is the thickness of the m^{th} layer.

The r_m and t_m are complex Fresnel coefficients for the m^{th} layer and is dependent on angle of incidence and polarisation (s or p -polarisation) [30]. This shows an example of formulation of the TMM to theoretically calculate reflection and transmission of thin-flim structures.

The FDTD was used to solve the maxwell's equations in a discretised domain. The staggered grid modelling the magnetic and electric field in alternative positions respectively in the cartesian coordinates. This is commonly known as the Yee grid approach introduced by Kanee Yee in 1966 [31].

The curl equations of the maxwells laws are solved at each grid point. The staggered grid approach allows for an intuitive numerical approximation of the curls of $\boldsymbol{E}$ and $\boldsymbol{H}$. It is related with the forward differencing time scheme for $\boldsymbol{B}$ and $\boldsymbol{D}$, equations (20) and (21). The same can be extended to all three axes. This is extended at a half time step as given by $\boldsymbol{E_x}|_{t+\Delta t/2}^{ijk}$ and $\boldsymbol{H_x}|_{t+\Delta t}^{ijk}$ using the formulation in equations (2), (3), (6), and (7).

$$\frac{\boldsymbol{H}_z|_t^{i+1} - \boldsymbol{H}_z|_t^i}{\Delta y} - \frac{\boldsymbol{H}_y|_t^{j+1} - \boldsymbol{H}_y|_t^j}{\Delta z} = \varepsilon . \frac{\boldsymbol{E}_x|_{t+\Delta t/2}^{ijk} - \boldsymbol{E}_x|_t^{ijk}}{\Delta t} \tag{20}$$

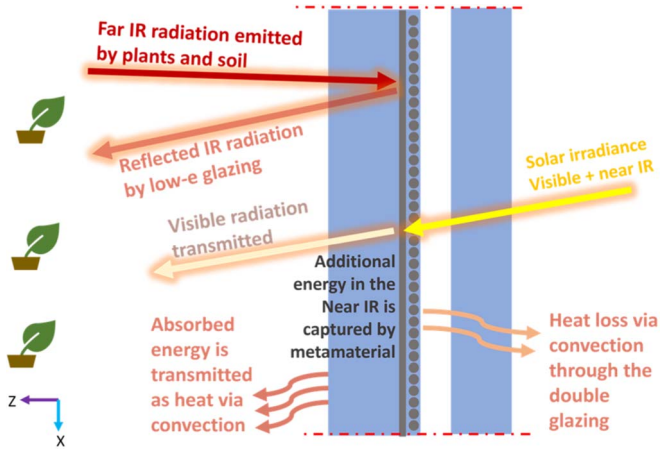

Figure 3. Double pane glazing structure-cross section and the expected transfer of light and heat (not to scale).

$$\frac{\boldsymbol{H}_z|^{i+1}_{t+\frac{\Delta t}{2}} - \boldsymbol{H}_z|^{i}_{t+\frac{\Delta t}{2}}}{\Delta y} - \frac{\boldsymbol{H}_y|^{j+1}_{t+\frac{\Delta t}{2}} - \boldsymbol{H}_y|^{j}_{t+\frac{\Delta t}{2}}}{\Delta z} = \mu.\frac{\boldsymbol{H}_x|^{ijk}_{t+\Delta t/2} - \boldsymbol{H}_x|^{ijk}_{t+\Delta t}}{\Delta t} \tag{21}$$

For each point in the centroid of the respective staggered meshes, $d(\nabla.\boldsymbol{B})/dt$ and $d(\nabla.\boldsymbol{D})/dt$ can be zero. By setting the initial conditions for the divergence term to zero. Then, the gauss's laws (equations (4) and (5)) are automatically satisfied by the Yee-grid approach [32].

The analysis was done using the FDTD module available in Ansys Lumerical 2023 R2 software package. The associated Ansys optics package also features a 1-D solver based on the transfer matrix method known as STACK. It allows for analysis with arbitrary angles of incidence and for both polarisations. The TMM analysis is done with the STACK module from the same package [33, 34].

A single silver NP embedded in SiO_2 is simulated with appropriate boundary conditions, planewave sources and material properties. This represents our proposed metamaterial design. The results from the thin film design simulations are validated against the results from the transfer matrix method. This serves as a general validation step for the FDTD setup. Periodic boundary conditions are imposed to faces in the direction along the glass surfaces for simulations with incidence normal to the glass surface. This condition equates the fields outside the domain to be equal to the fields on the opposite face for normal irradiance and transmittance.

The field transformation technique outlined by liang *et al* implemented in Ansys optics FDTD as the 'BFAST' option is used [35]. This is more suited to broad band simulations for plane wave incidents with periodic boundaries [36]. This reduces the maximum time step criteria given as in equation (22) increasing computational time.

$$\Delta t' = \Delta t(1 - \sin\theta)/\sqrt{3} \tag{22}$$

The perfectly matched layers (PML) are used to fully absorb the incident waves. No reflection was observed in all cases. Plane wave sources inject pulses of electric field in the time domain in the frequencies of interest. The transmittance and reflectance measurements are related with the spectral distribution of the pulse [37]. The total domain of the FDTD analysis in Ansys Lumerical are shown in figures 4 and 5, respectively.

The material properties for glass are from the refractive index database from [38]. The in-built material properties of silver are from the inbuilt database compiled from Handbook of Optical Constants of Solids.

For the FDTD simulations, multi coefficient models (MCM) are based on guidelines from Ansys [39]. This involved fitting the refractive index data against the model using an in-built tool inside of Lumerical. The fit parameters are tuned until adequate fit was obtained. Due to the limited availability of the material properties of silver in the longer wavelengths, the simulation bandwidth was limited to 3–10 μm.

The numerical wave velocity accuracy i.e., accuracy of the simulation in the finite difference model is dependent on grid density per wavelength of light. The wave velocity anisotropy, i.e., the variation of wave velocity at various angles of propagation is also a key factor in determining the grid density.

The numerical velocity approaches the 100% of the velocity of light in the medium when the maximum mesh size is given by equations (23) and (24). SiO_2 glass has an effective refractive index of 1.55 at visible wavelengths [40]. Thus, the maximum cell size for simulating glazing structures is maintained to be less than

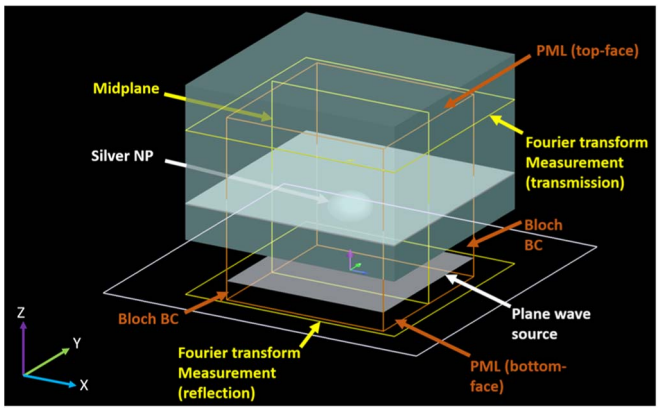

Figure 4. Domain of the simulation in the FDTD software.

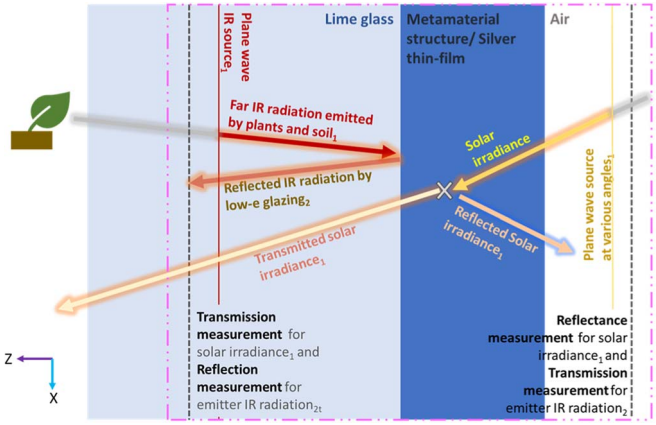

Figure 5. The glazing cross-section.

19 nm.

$$\lambda \times n = \lambda_0 \tag{23}$$

$$\Delta x < \frac{\lambda}{10} \tag{24}$$

The conformal meshing method is developed in Ansys FDTD solver based on the Yu-Mittra method. This formulates the effective complex refractive index in the cells at interfaces. This allows for a more accurate resolution of sub-cell features in the edge cells especially for the plasmonic particles. The 'conformal variant 1' option is used [41, 42].

The graded mesh option was used which reduces the mesh size close to the interfaces in the areas with higher refractive indices (figure 6). This reduces the error in the modelled thickness of thin film structures and NP boundaries.

The courant number stability criterion gives the maximum time step size for the FDTD simulation [43]. The chosen time step was 90% of the time step given by equation (25). A grid convergence study is performed to arrive at computationally practical and sufficiently accurate mesh size.

$$\Delta t \leqslant \frac{\Delta x}{\sqrt{3}\,c} \tag{25}$$

The deviations in the transmission and reflectance profiles against the most refined mesh are shown in figures 7 and 8. Based on the convergence of the spectral characteristics, the 30 cells per wavelength level of mesh size was sufficient since less than 1% average change in the spectrum was observed beyond this refinement level. The spectral reflection and transmission curves also converged as shown in figures 7– 9, respectively.

The spectral reflectance and transmittance for both the TMM and FDTD methods for the thin film case are shown in figures 10 and 11. Deviations were observed at longer wavelengths for both inclined irradiance and

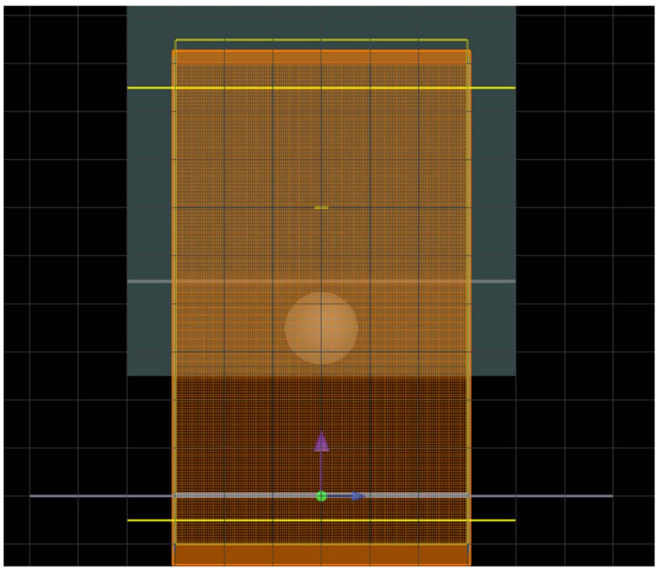

Figure 6. Generated mesh for FDTD analysis.

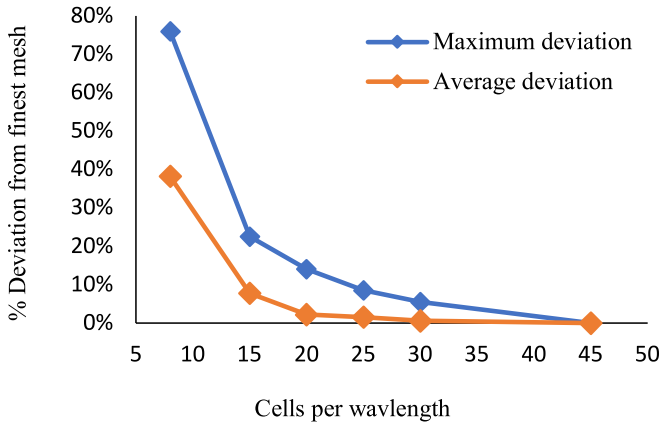

Figure 7. Deviation in transmittance spectrum against most refined mesh.

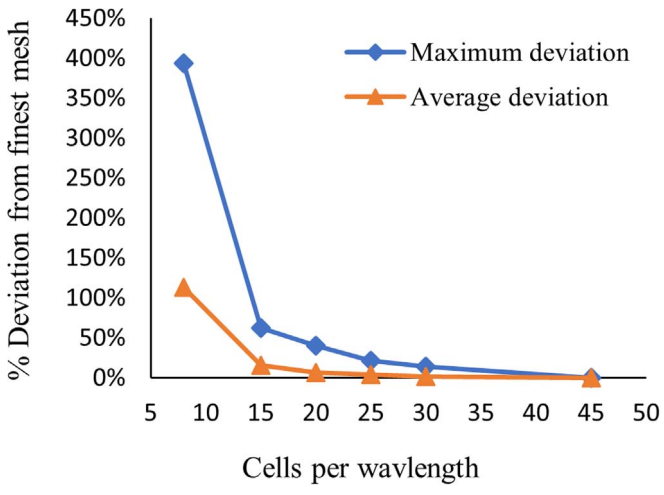

Figure 8. Deviation in reflectance against most refined mesh.

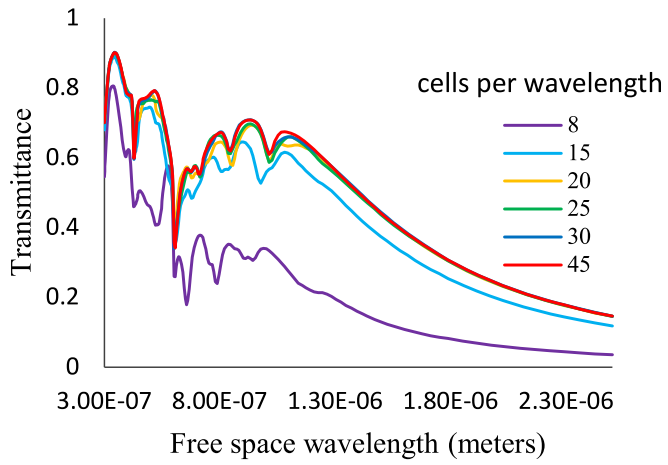

Figure 9. Spectral transmittance of the test case at various mesh sizes.

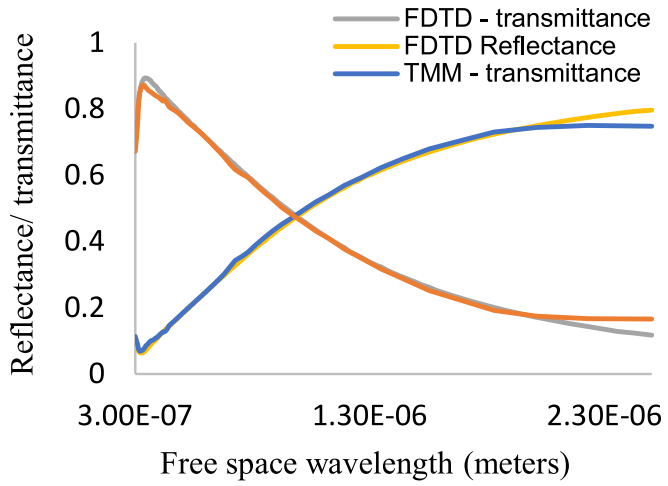

Figure 10. Verification of the FDTD results against TMM for normal irradiance.

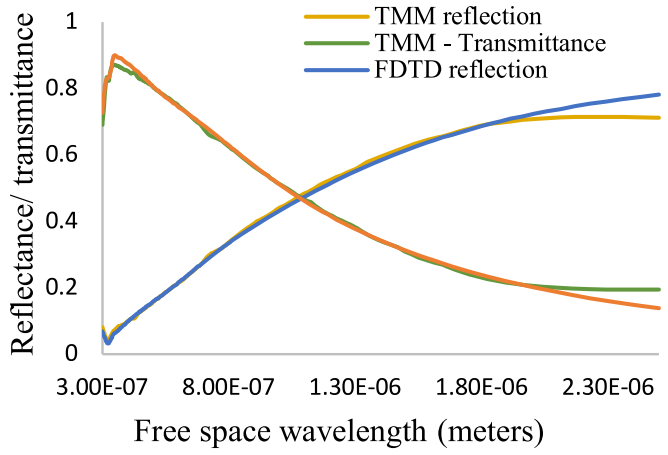

Figure 11. Verification of the FDTD results against TMM for 30° inclined irradiance.

normal irradiance. Any additional refinement in mesh or increase in the number of PML layers is not yield to the different results. Given the overall agreement between the TMM and FDTD for both inclined irradiance and normal irradiance, the FDTD model was sufficiently robust for this work.

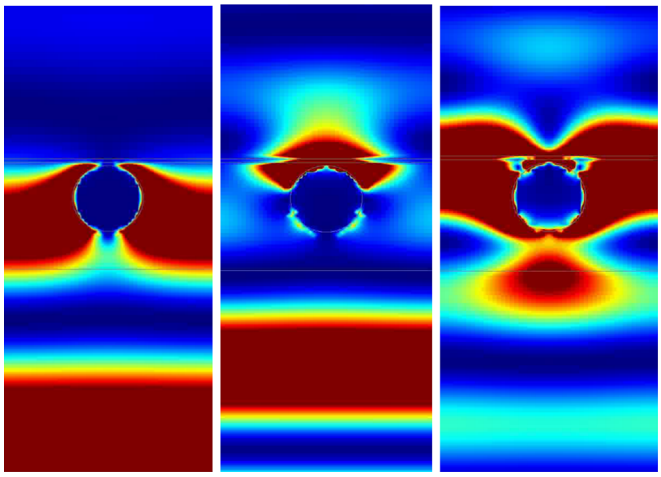

Figure 12. Sequence of contours of electric field showing the pulse interacting with the NP and the thin film. (The contour colours are only illustrative of the electric field as it moves across the cross section).

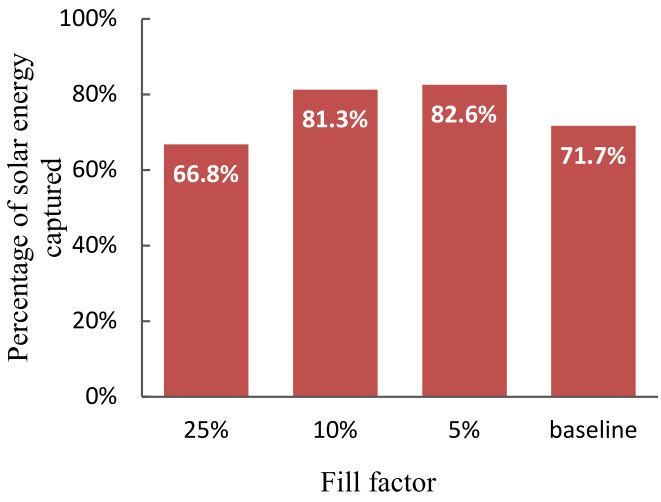

Figure 13. Comparison of total solar energy captured at various fill-factors.

To evaluate the overall performance of the glazing the total admitted power, i.e., total solar energy captured by transmittance or glazing was calculated using equation (26). This does not consider heat transfer losses such as convection losses but only accounts for the radiation performance of the coating.

$$\begin{gathered} Total\ admitted\ power = \sum (1 - R(\lambda))\ *\ P_{solar}(\lambda)\ *\ \Delta\lambda \\ \Delta\lambda \rightarrow spectral\ sample\ width \\ P_{solar}(\lambda) - Spectral\ power\ of\ solar\ irradiance \\ R(\lambda) - Spectral\ reflectance\ of\ glazing \end{gathered} \tag{26}$$

3. Results

The overall effect of the NP visualisation is presented in figure 12 to shows the electric field magnitude contours at the cross-section of the midplane of y-axis in figure 4. This shows a visual view of the pulse passing through the domain interacting with the NP. Strong field enhancement between the NP and the silver thin film is visualised showing the working principle.

The effect of fill-factor is studied by simulating the 150 nm nanoparticle with 5%, 10%, and 25% effective cross-sectional area ratios. The fill factor of 5% shows the highest admittance of the solar radiation, capturing 10% more energy than the 10%, and 25% fill factor as shown in figure 13.

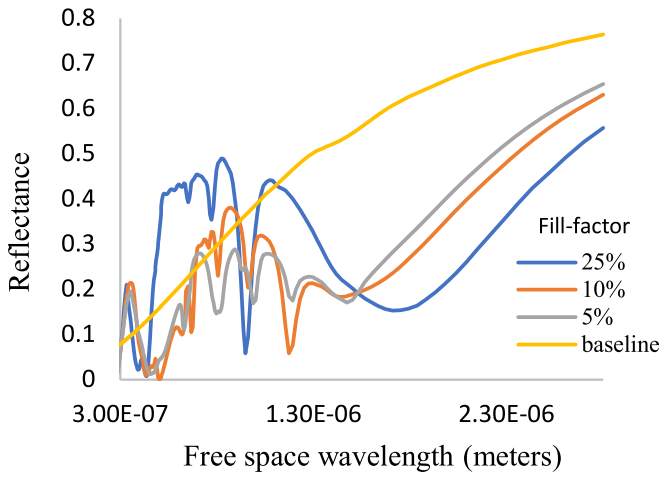

Figure 14. Spectral reflectance of solar radiation at various fill factors.

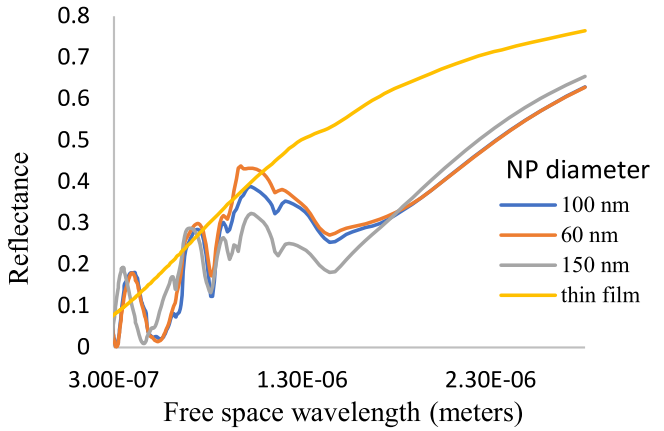

Figure 15. Spectral reflectance of solar radiation at various NP sizes.

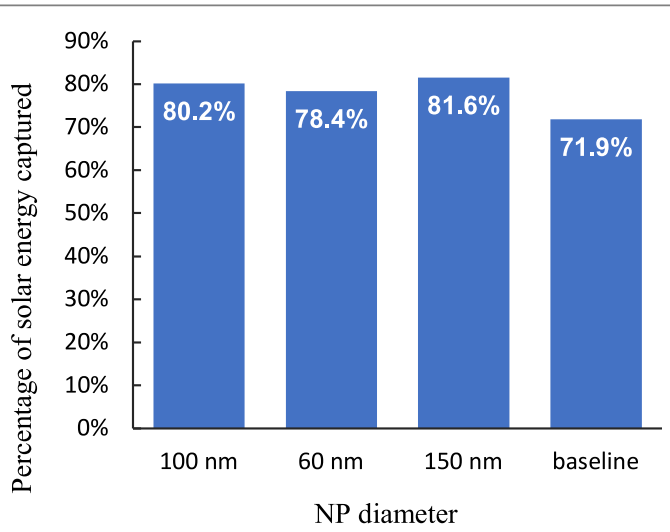

Figure 16. Comparison of total solar energy captured with various NP sizes.

Figure 14 shows the reflectance against free space wavelength. It was observed that at higher fill factors, the reflectance is higher especially in the visible/PAR range. The denser arrangement of silver NPs is observed to function as a reflective layer instead of improving admittance.

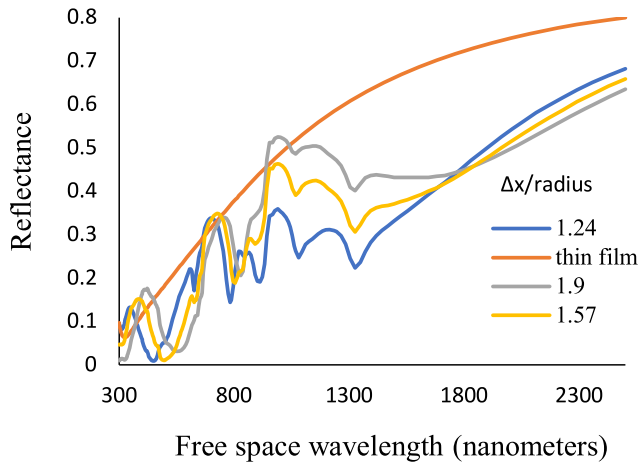

Figure 17. Spectral reflectance of solar radiation at various distances to thin film.

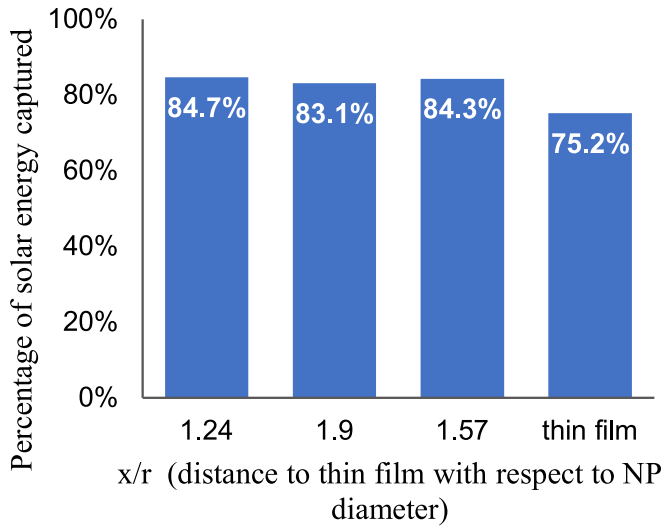

Figure 18. comparison of total solar energy captured at different distances to thin-film.

The effect of particle size on the reflectance spectrum is depicted in figure 15. The fill factor is considered at 5% for all cases and the distance to thin film for a given particles size, i.e., ***x/radius*** is constant at 1.57. Figure 16 shows the solar energy percentage captured against NP diameter. It was observed that larger NP shows improved response at longer wavelengths and higher overall admittance . This is attributed to the greater activity of larger diameter NPs in longer wavelengths, as explained by Mie scattering theory [44].

The effect of distance from thin film, i.e., Δx/radius for 1.24, 1.57, 1.9 is shown in figures 17 and 18. It was observed that when the NP is closer to the thin film, it has a higher solar admittance. This can be due to the increased activity between the thin film and the NPs due to the proximity increasing admittance.

The comparison of the inclined illumination of the thin film baseline case and metamaterial is presented in figure 19 against normal illumination. The parameters for the simulation are 5% fill factor, and 150 nm diameter NP at $\Delta x/radius$ of 1.57. At inclined illumination the reflectance is higher as predicted by the Fresnel equations. This is observed for both the thin film design and the metamaterial design. Future work would focus on investigating different inclined radiation angles to have insights in its effect on the metamaterial.

The low-e performance of the metamaterial glazing (i.e. transmittance and reflectance from the inside to the outside) along with the existing thin film design is shown in figures 20 and 21. Since, there are no changes on the inside thin film structure both the glazing design performs similarly as expected.

The transmittance of the metamaterial design and the thin film baseline is shown in figure 22. There is no significant loss in the PAR thus the glazing does not adversely affect plant health by reducing solar irradiance for photosynthesis.

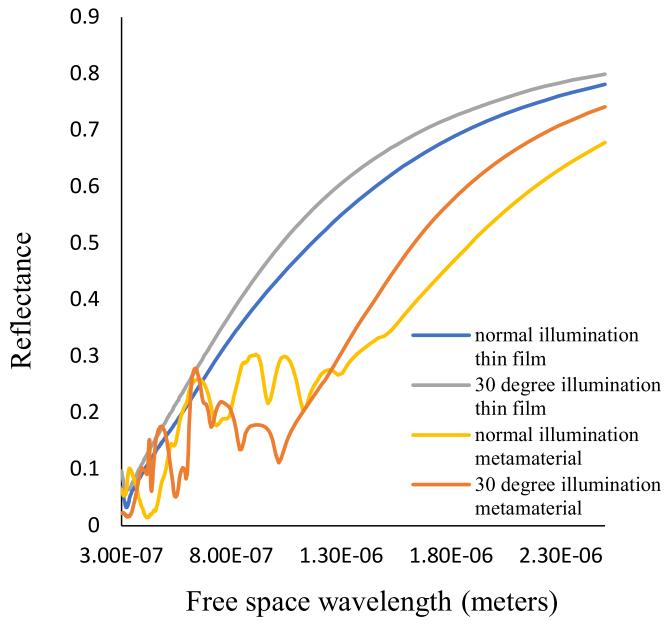

Figure 19. Comparison of spectral reflectance of solar radiation at normal and inclined illumination.

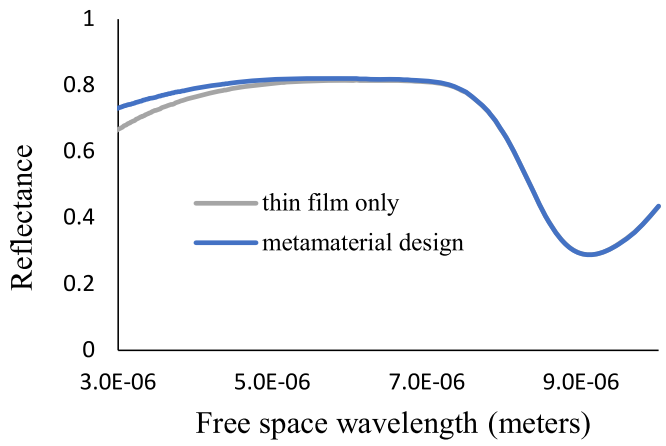

Figure 20. Spectral reflectance from inside the glazing to outside.

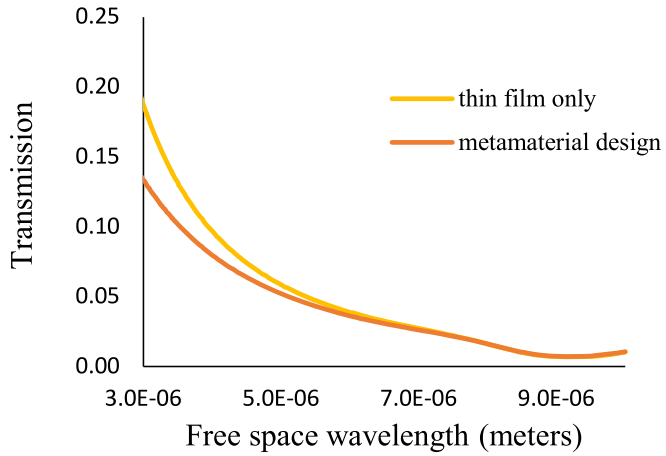

Figure 21. Spectral transmittance from inside the glazing to outside.

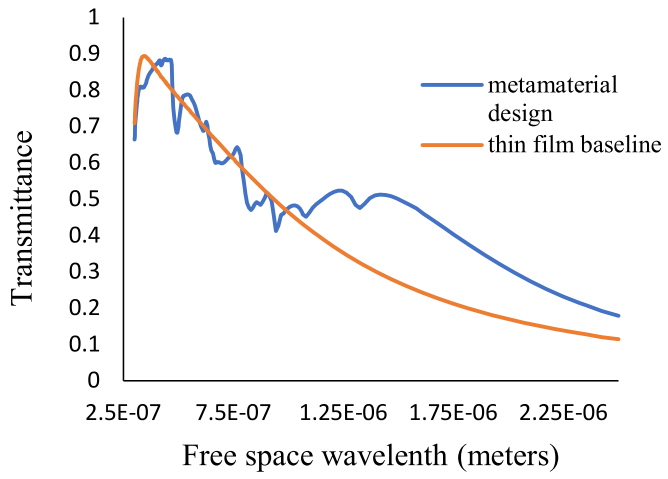

Figure 22. Spectral transmittance of solar irradiance of metamaterial design.

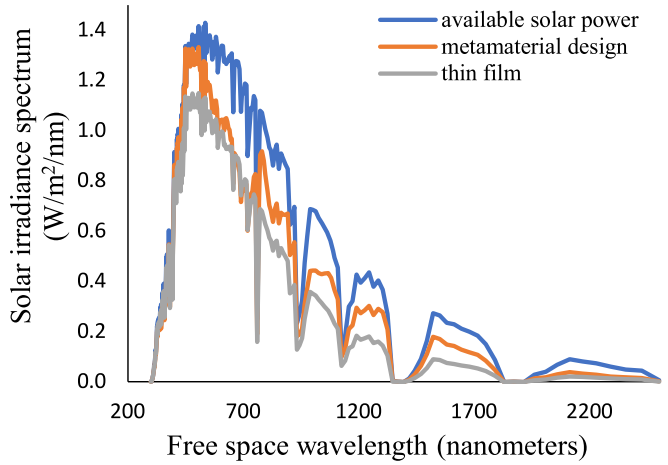

Figure 23. Total available solar energy and the captured energy.

Table 2. Comparison of results with existing studies.

Design	Improvement over baseline (in each case)	Remarks	References
Silver nano-particles embedded in SiO_2 matrix	11% improvement over thin film low-e design	Based on ISO:9050 standard procedure to calculate glazing efficiency	This study
Lithography based silver checkerboard pattern with Ag thin film	The authors report a maximum of 220 W m^{-2} and 94 W m^{-2} of additional energy captured while maintaining high visible light transmittance	Results are based on similar FDTD simulations. By varying the parameters of the design, the authors show control over the spectral transmittance and reflectance	[19]
Cu nano disks with Ag thin film	The authors report a 25% difference in the absorption of energy between the outside and the inside	Experimental study on a small plain glass	[45]

The total power captured was calculated against the available solar power (AM1.5) as shown in figure 23. More of the available energy especially in the longer wavelengths is captured by the meta-surface design achieving the aim the of the design.

A comparison of the results with similar studies is presented in table 2. The designs and methodologies are similar. However, direct comparison of the results is not possible due to difference baselines selection, and effectiveness calculation procedure of the proposed metamaterial gazing. The advantage of our approach is adaptation of the ISO:9050 standard procedure to calculate glazing efficiency. However, all three designs shows improvement in capturing additional solar radiation.

4. Conclusion and future works

The metamaterial design proposed is shown to improve capture of additional solar energy normally wasted by low-e glass. Similar performance to the design proposed by [19], but using NPs that can be fabricated on a larger scale has been shown. The total effectiveness of the design is 11% improvement over the thin-film low-e design, based on the calculation procedures given by the ISO:9050 standard.

The optimal parameters based on the performed simulations that captures maximum energy are 150nm diameter nanoparticles placed closest to the thin film with a low fill factor of 5%. The design also performed robustly when subjected to variations, except for fill factor. The performance of the low emissivity function of the thin film coating is not affected negatively by the NPs. It should be noted that selecting the optimum glazing design often involves decisions specific to the greenhouse system including factors like cost, weather, energy use, environmental goals, and availability of other control systems.

Careful control of distribution over the glazing area is required, because high density of NP lead to worse performance than the baseline thin film. There may be also complex resonance modes in between the particles itself which will not be captured with the methodology used in this report. Full simulation of a random distribution of NPs like the work done by [44], overcoming the computational limitations is an interesting topic for future work. The NP coatings performed without loss in inclined irradiance. However, analysis of the design parameters at various irradiance and the effect of irradiance inclination are areas of further studies. Such glazing designs may also prove useful in other applications such as solar thermal capture and building glazing in cold climates apart from greenhouses where maxmising the capture of the solar energy is useful.

This article presents only a theoretical approach to optical glazing design however real-world performance of the glazing may differ significantly from the theoretical results [11, 18]. So, validation of the results with experimental data will prove both the accuracy of the simulations as well as demonstrate the practicality of fabricating unstructured metamaterials.

Acknowledgments

This work incorporates contributions that were initially developed as part of a Master's thesis at Cranfield University. The authors would like to express their gratitude to the faculty and staff of Cranfield University for their guidance and support throughout the course of this research.

Furthermore, we would like to clarify that there were no external funding sources for this research. All resources utilized were provided by the authors themselves. This ensured that the research was conducted without any potential conflicts of interest related to funding sources.

Data availability statement

All data that support the findings of this study are included within the article (and any supplementary files).

ORCID iDs

Mostafa Ranjbar https://orcid.org/0000-0002-9670-7371
Khalifa Aliyu Ibrahim https://orcid.org/0000-0001-8404-8359
Zhenhua Luo https://orcid.org/0000-0003-0766-6174

References

[1] Research and Markets 2022 *United Kingdom (UK) Commercial Greenhouse Market Overview, 2027*
[2] Gorjian S, Calise F, Kant K, Ahamed M S, Copertaro B, Najafi G, Zhang X, Aghaei M and Shamshiri R R 2021 A review on opportunities for implementation of solar energy technologies in agricultural greenhouses *J. Clean. Prod.* **285** 124807
[3] Semple L, Carriveau R and Ting D S-K 2017 Assessing heating and cooling demands of closed greenhouse systems in a cold climate *Int. J. Energy Res.* **41** 1903–13
[4] Yoon S-M 2022 On the interdependence between biofuel, fossil fuel and agricultural food prices: Evidence from quantile tests *Renew Energy* **199** 536–45
[5] Hemming S, Kempkes F L K and Mohammadkhani V 2011 New glass coatings for high insulating greenhouses without light losses - energy saving, crop production and economic potentials *Acta Hortic.* 217–26
[6] Bakos G C, Fidanidis D and Tsagas N F 1999 Greenhouse heating using geothermal energy *Geothermics* **28** 759–65
[7] Gansel J K, Thiel M, Rill M S, Decker M, Bade K, Saile V, von Freymann G, Linden S and Wegener M 2009 Gold Helix Photonic Metamaterial as Broadband Circular Polarizer *Science* **325** 1513–5
[8] Yang C, Niu S, Chang H, Wang Y, Feng Y, Zhang Y, Li G, Chen S, Qu Y and Xiao L 2021 Thermal infrared and broadband microwave stealth glass windows based on multi-band optimization *Opt. Express* **29** 13610

[9] Farhangdoust S, Adediran I A, Ranjbar M and Krushynska A O 2021 Vibro-acoustic analysis of auxetic hexagonal and anti-tetrachiral stepped cantilever beams *Health Monitoring of Structural and Biological Systems XV* (SPIE)
[10] Mostafa R 2023 *A review on the applications of auxetics in vibroacoustic design optimization of structures UK Metamaterials Int. Conf. 2023* (Manchester) Metropolitan University
[11] Zhai Y, Ma Y, David S N, Zhao D, Lou R, Tan G, Yang R and Yin X 2017 Scalable-manufactured randomized glass-polymer hybrid metamaterial for daytime radiative cooling *Science* **355** 1062–6
[12] Tani T, Hakuta S, Kiyoto N and Naya M 2014 Transparent near-infrared reflector metasurface with randomly dispersed silver nanodisks *Opt. Express* **22** 9262
[13] Gerislioglu B, Dong L, Ahmadivand A, Hu H, Nordlander P and Halas N J 2020 Monolithic Metal dimer-on-film structure: new plasmonic properties introduced by the underlying metal *Nano Lett.* **20** 2087–93
[14] Cerjan B, Gerislioglu B, Link S, Nordlander P, Halas N J and Griep M H 2022 Towards scalable plasmonic Fano-resonant metasurfaces for colorimetric sensing *Nanotechnology* **33** 405201
[15] Huh J, Kim K, Im E, Lee J, Cho Y and Lee S 2020 Exploiting colloidal metamaterials for achieving unnatural optical refractions *Adv. Mater.* **32** 2001806
[16] Moon J H, Ford J and Yang S 2006 Fabricating three-dimensional polymeric photonic structures by multi-beam interference lithography *Polym. Adv. Technol.* **17** 83–93
[17] Dintinger J, Mühlig S, Rockstuhl C and Scharf T 2012 A bottom-up approach to fabricate optical metamaterials by self-assembled metallic nanoparticles *Opt. Mater. Express* **2** 269
[18] Li T, Gao Y, Zheng K, Ma Y, Ding D and Zhang H 2019 Achieving Better Greenhouse Effect than Glass: Visibly Transparent and Low Emissivity Metal-Polymer Hybrid Metamaterials *ES Energy & Environment* **5** 102–7
[19] Heltzel A, Mann T and Howell J R 2018 Metamaterial window glass *J Therm Sci Eng Appl* **10** 051010–1 TSEA-15-1130
[20] NREL Reference *Air Mass 1.5 Spectra* (National Renewable Eenergy Labaratory)
[21] Papadakis G, Briassoulis D, Scarascia Mugnozza G, Vox G, Feuilloley P and Stoffers J A 2000 Review paper (SE—structures and environment) *J. Agric. Eng. Res.* **77** 7–38
[22] Carruthers T J B, Longstaff B J, Dennison W C, Abal E G and Aioi K 2001 Measurement of light penetration in relation to seagrass *Global Seagrass Research Methods* (Elsevier) 369–92
[23] Ding G and Clavero C 2017 Silver-based low-emissivity coating technology for energy- saving window applications *Modern Technologies for Creating the Thin-film Systems and Coatings ed Nikolay Nikitenkov* (Croatia: InTech) 409–23
[24] Baryshnikova K V, Petrov M I, Babicheva V E and Belov P A 2016 Plasmonic and silicon spherical nanoparticle antireflective coatings *Sci. Rep.* **6** 22136
[25] Kurihara K, Rockstuhl C, Nakano T, Arai T and Tominaga J 2005 The size control of silver nano-particles in SiO2 matrix film *Nanotechnology* **16** 1565–8
[26] Fan X, Zheng W and Singh D J 2014 Light scattering and surface plasmons on small spherical particles *Light: Sci. Appl.* **3** e179–179
[27] Polyanskiy M N 2023 Refractiveindex.info database of optical constants *Sci. Data* **11** 94
[28] Jenkins F A and Harvey E W 2001 *Fundametals of Optics* ed A F Robert and T Anne *Vinnicombe* (McGraw-Hill Custom Publishing)
[29] Chakrabarti S 2019 Determination of The Damping Co-Efficient Of Electrons In Optically Transparent Glasses At The True Resonance Frequency In The Ultraviolet From An Analysis Of The Lorentz-Maxwell Model of Dispersion submitted (arXiv:1907.04499)
[30] Heavens O S 1991 *Optical Properties Of Thin Solid Films* (Dover Publications Inc)
[31] Kane Yee 1966 Numerical solution of initial boundary value problems involving maxwell's equations in isotropic media *IEEE Trans. Antennas Propag.* **14** 302–7
[32] Purdue University Finite Difference Method, Yee Algorithm
[33] Ansys STACK Optical Solver Overview
[34] Ansys FDTD product reference manual
[35] Liang B, Bai M, Ma H, Ou N and Miao J 2014 Wideband analysis of periodic structures at oblique incidence by material independent FDTD algorithm *IEEE Trans. Antennas Propag.* **62** 354–60
[36] Ansys Optics Broadband Fixed Angle Source Technique (BFAST) *Ansys Optics*
[37] Ansys Optics Plane wave and beam source - Simulation object *Ansys Optics*
[38] Rubin M 1985 Optical properties of soda lime silica glasses *Sol. Energy Mater.* **12** 275–88
[39] Ansys Lumerical Overcoming the Multi-wavelength FDTD Challenge *Ansys Lumerical*
[40] Johnson P B and Christy R W 1972 Optical constants of the noble metals *Phys. Rev.* B **6** 4370–9
[41] Yu W, Mittra R, Arakaki D and Werner D H 1997 A Conformal Finite Difference TIme Domain (CFDTD) Algorithm For Modelling Perfectly Conducting Objects *IEEE Microwave and Guided Wave Letters,* **7** 273–5
[42] Ansys Optics Selecting the best mesh refinement option in the FDTD simulation object *Ansys Optices*
[43] Sullivan D M 1996 Exceeding the courant condition with the FDTD method *IEEE Microw. Guid. Wave Lett.* **6** 289
[44] Naruse M, Tani T, Yasuda H, Tate N, Ohtsu M and Naya M 2014 Randomness in highly reflective silver nanoparticles and their localized optical fields *Sci. Rep.* **4** 6077
[45] Ma R, Wu D, Liu Y, Ye H and Sutherland D 2020 Copper plasmonic metamaterial glazing for directional thermal energy management *Mater. Des.* **188** 108407